metals

MDPI

Article

Control of Macrosegregation in Titanium Alloy VAR Ingots via Alternating Magnetic Fields: Governing Roles of Field Strength and Frequency

Meirong Jiang [1,2], Yulun Wu [1,3], Qing Wang [1,4], Jie Fu [1,3], Jinjin Shang [1], Tao He [1], Longchao Huang [1], Kaixuan Wang [1], Zhongqiu Liu [2] and Xianghong Liu [5,*]

[1] Western Superconducting Technologies Co., Ltd., Xi'an 710018, China
[2] School of Metallurgy, Northeastern University, Shenyang 110819, China
[3] State Key Laboratory of Solidification Processing, Northwestern Polytechnical University, Xi'an 710072, China
[4] School of Physical Science and Technology, Northwestern Polytechnical University, Xi'an 710072, China
[5] Northwest Institute for Non-Ferrous Metal Research, Xi'an 710016, China
* Correspondence: xhliu@c-wst.com

Abstract

Vacuum arc remelting (VAR) is essential for producing premium titanium alloys, where an externally applied alternating magnetic field enables circumferential stirring to control ingot homogeneity. However, current magnetic field parameter design relies on empirical trial-and-error approaches, lacking systematic theoretical guidance. To address this issue, this study establishes a comprehensive multi-physics framework through a two-dimensional axisymmetric swirl model integrating electromagnetic, fluid dynamics, thermal, and solute transport phenomena. Our findings demonstrate that both the magnetic field strength and period exhibit optimal operating ranges, which directly influence ingot homogeneity. As magnetic field strength increases progressively, ingot uniformity shows a distinctive non-monotonic response—initially improving before subsequently deteriorating. Correspondingly, with increasing stirring period, macrosegregation undergoes a distinct three-stage evolution: initial mitigation, subsequent aggravation, and final alleviation. These phenomena originate from the small-scale circulatory flow generated by the external magnetic field on the surface of the VAR molten pool. The interactions among the flow, the solute diffusion layer, and the mushy zone collectively alter elemental diffusion behavior, ultimately determining the homogeneity of the ingot. This study provides a theoretical foundation for precise control of ingot homogeneity in titanium alloy VAR processes and demonstrates significant potential for engineering applications.

Keywords: macro-segregation; titanium alloy; vacuum arc remelting; alternating magnetic fields; numerical simulation

Check for updates

Academic Editors: Maciej Motyka and Abdollah Saboori

Received: 23 February 2026
Revised: 23 March 2026
Accepted: 1 April 2026
Published: 20 April 2026

Copyright: © 2026 by the authors. Licensee MDPI, Basel, Switzerland. This article is an open access article distributed under the terms and conditions of the Creative Commons Attribution (CC BY) license.

1. Introduction

Titanium alloys have emerged as critical structural materials in high-end applications such as aerospace (e.g., engine blades, airframe structures) and biomedical (e.g., implants) fields, owing to their high specific strength, excellent corrosion resistance, and good biocompatibility [1–3]. However, their high chemical reactivity makes them prone to react with interstitial elements such as O and N during melting, forming brittle compounds (e.g., TiO_2, TiN) [4–6]. Vacuum arc remelting, characterized by relatively low equipment

investment, precise composition control, and high process reproducibility, has become the leading technique for producing high-quality titanium alloy ingots [7–10].

In VAR processes, the persistent redistribution of solute elements during solidification, coupled with complex thermosolutal convection within the mushy zone, frequently leads to macrosegregation defects in the final ingot—manifested as inhomogeneous distribution of alloying elements (e.g., iron, nickel, zirconium) along both axial and radial directions [11–15]. To mitigate such macrosegregation, the application of an externally applied alternating magnetic field has emerged as a common industrial practice, as shown in Figure 1a. The externally imposed axial magnetic field induces circumferential electromagnetic (Lorentz) forces, which directly modify molten pool flow patterns and solidification behavior, thereby offering a promising route to alleviate segregation-related defects [16–19].

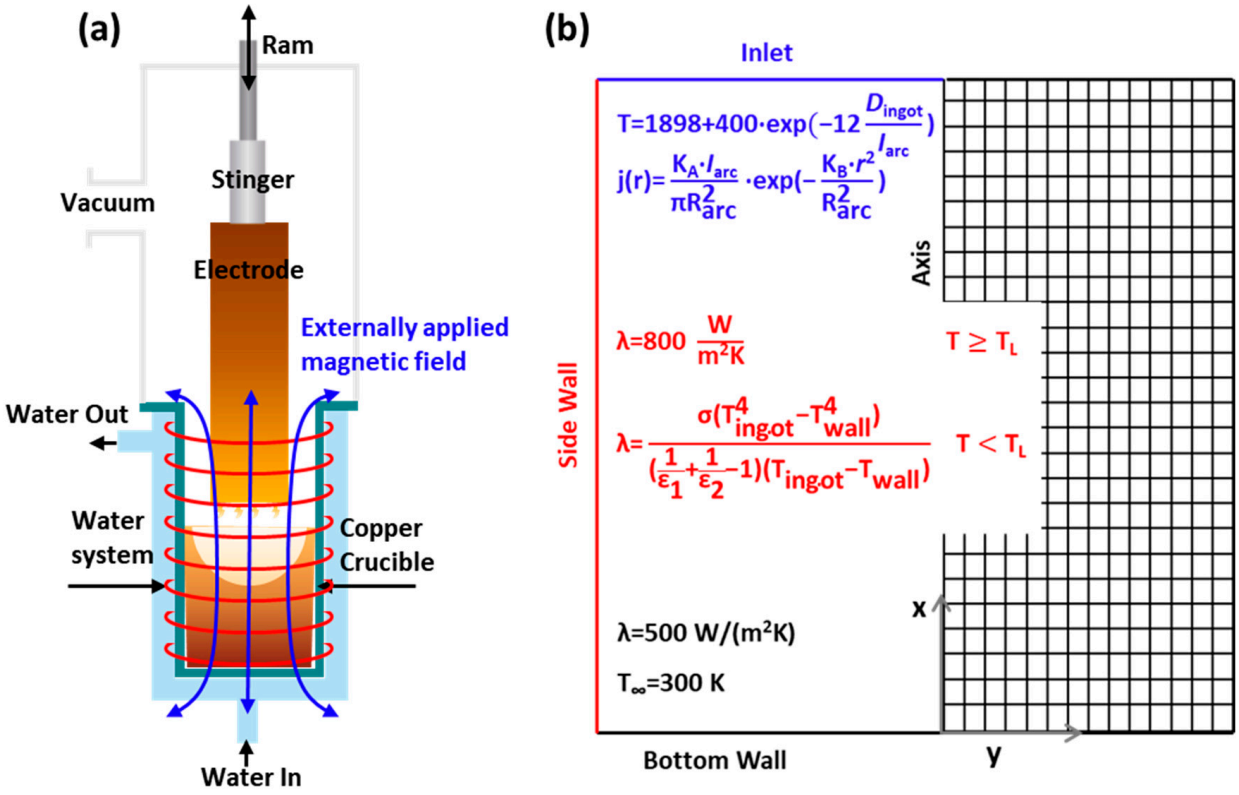


Figure 1. (**a**) Schematic representation of the VAR process; (**b**) Cross-sectional view of the VAR setup, showing different regions and boundaries, including the ingot, mold, and the applied thermal and electromagnetic boundary conditions.

Existing research has demonstrated that an applied stirring magnetic field can effectively mitigate ingot macrosegregation [20–23]. Numerical simulations by Karimi-Sibaki, Xiong et al. [21,24,25] revealed that while the molten pool reaches its maximum depth and exhibits severe macrosegregation without external magnetic fields, the application of magnetic stirring reduces pool depth, with this effect becoming increasingly pronounced at higher field strengths, thereby mitigating segregation. Subsequently, simulations by Han et al. [20,22,23,26,27] indicated that an external axial magnetic field can effectively ameliorate macrosegregation in the ingot compared to scenarios without such a field.

Recently, Sun et al. [28,29] provided experimental confirmation that an externally applied magnetic field indeed reduces pool depth. Furthermore, at a constant magnetic field strength, a lower frequency results in a shallower pool. Paradoxically, experiments and simulations by Mramor et al. [30] suggested that increasing the intensity and cycling period of a strong stirring magnetic field can exacerbate macrosegregation. In summary,

while existing studies confirm that an external stirring magnetic field can improve ingot macrosegregation, some evidence indicates that strong stirring fields may aggravate it. Consequently, the critical magnetic field strength and frequency parameters required to reduce macrosegregation, as well as the precise relationship between field parameters and segregation severity, remain poorly understood and warrant systematic investigation.

Furthermore, direct experimental observation of the solidification process during vacuum arc remelting (VAR) is impractical due to the extreme high-temperature conditions and dynamic nature of the process within a vacuum environment. Furthermore, the economic cost associated with industrial-scale melting and full ingot dissection—often amounting to several hundred thousand RMB per ingot—renders experimental approaches prohibitively expensive. Fortunately, advances in numerical simulation techniques now offer an effective and economically viable alternative to replicate the solidification dynamics of the VAR process [31–37].

Thus, this study employs a numerical modeling approach to simulate the solidification of a VAR-processed ingot. Using a Ti-Al binary alloy as a model system, we adopt a two-dimensional axisymmetric model that accounts for circumferential fluid flow. Through systematic numerical investigations, we aim to elucidate the influence of alternating magnetic field strength and frequency on macrosegregation patterns in the final ingot. The work further seeks to uncover the underlying mechanisms by which electromagnetic stirring impacts compositional distribution and to establish quantitative correlations between alternating magnetic field parameters and the degree of macrosegregation.

Consequently, this work develops a comprehensive multi-physics modeling framework based on a two-dimensional axisymmetric swirl model that systematically integrates electromagnetic fields, fluid dynamics, heat transfer, and solute transport phenomena. The established framework enables high-fidelity simulation of solidification behavior during VAR of titanium alloys. Focusing on a Ti-Al binary system as a model material, we systematically investigate the effects of alternating magnetic field strength and period on ingot homogeneity while revealing the underlying mechanisms through which these parameters govern segregation patterns. The findings provide crucial theoretical support and demonstrate significant engineering potential for advancing the manufacturing of premium titanium alloys.

2. Modeling

Given that the primary objective of this work is to elucidate the effect of an external alternating magnetic field on macrosegregation during VAR of titanium alloy ingots, we employ a Ti-Al binary alloy system. This system is simpler than the multicomponent alloys used in industrial production, with an initial aluminum concentration of 6 wt.%. The VAR process is modeled using the continuum formulation proposed by Bennon et al. [38–41], which considers only laminar flow and neglects turbulence.

2.1. Governing Equations

In the present study, the governing equations are formulated as follows.

(1) Mass continuity equation:

$$\nabla \cdot \left(\rho \vec{v} \right) = 0 \tag{1}$$

where ρ indicates density, $\vec{v}$ is the velocity vector.

(2) Momentum conservation equation:

$$\rho\left[\frac{\partial \vec{v}}{\partial t}+\left(\vec{v}\cdot\nabla\right)\vec{v}\right]=-\nabla p+\nu\nabla^2\vec{v}+\rho\vec{g}+\vec{F} \tag{2}$$

where p is the static pressure, ν is viscosity, and $\vec{g}$ is the gravitational body force. $\vec{F}$ represents external body forces, which includes solute buoyancy and electromagnetic force, and its form is as follows:

$$F=\rho\left[\beta_s\left(c_l-c_{ref}\right)\right]+\vec{j}\times\vec{B} \tag{3}$$

$$\vec{j}=-\sigma\cdot\nabla\varphi;\ \vec{B}=\nabla\times\vec{A} \tag{4}$$

$$\nabla\cdot(\sigma\nabla\varphi)=0;\ \nabla^2\vec{A}=-\mu_0\vec{j} \tag{5}$$

where β_s indicates the solute expansion coefficient, c_l denotes the instantaneous solute concentration in the liquid phase, c_{ref} is the reference solute concentration, and $\vec{j}$ and $\vec{B}$ represent the current density and the magnetic flux density vector, respectively. σ denotes the electrical conductivity, φ stands for the electric potential, $\vec{A}$ indicates the magnetic vector potential, and μ_0 is permeability of free space.

(3) Energy equation:

$$\frac{\partial}{\partial t}(\rho h)+\nabla\cdot\left(\rho h\vec{v}\right)=\nabla\cdot(k\nabla T)-\nabla\cdot[\rho(h_l-h)\vec{v}] \tag{6}$$

where h is sensible enthalpy, k is thermal conductivity, and T indicates the temperature.

(4) Species transport equation:

$$\frac{\partial}{\partial t}(\rho c_l)+\nabla\cdot\left(\rho\vec{v}c_l\right)=\nabla\cdot(D_l\nabla c_l)+\rho(1-k)\cdot\frac{\partial}{\partial t}(f_s c_l) \tag{7}$$

In addition, during the VAR process, the enthalpy-porosity technique is employed to treat the mushy zone (where part of the material is melted and part remains solid) as a porous medium. In this model, the porosity of each computational cell is set equal to its liquid fraction, ranging from 0 to 1. A porosity of 0 indicates a fully solid cell where flow is not solved, while a porosity greater than 0 indicates a partially liquid cell where fluid flow is permitted but with modified characteristics compared to the fully liquid region. By solely relying on the variation in porosity, this approach effectively captures the solidification behavior from liquid to solid during the VAR process of titanium alloys. Due to the reduced porosity in the mushy zone, a source term is introduced into the momentum equation as follows [42]:

$$S=\frac{(1-f)^2}{(f^3+q)}A_{\text{mush}}\vec{v} \tag{8}$$

where f is the liquid volume fraction, q is a small number (0.001) used to prevent division by zero, and A_{mush} is the mushy zone constant. The mushy zone constant A_{mush} represents the flow resistance magnitude in the mushy region; a higher value leads to a larger velocity gradient during melting or solidification. An excessively large value may cause divergence. In this study, the mushy zone constant is set to 6.46×10^{-6}, corresponding to a primary dendrite arm spacing of 0.8 mm.

2.2. Geometric Model and Boundary Conditions

In the solidification process of VAR ingots, melt flow is simultaneously driven by two mechanisms: a recirculating flow induced by electromagnetic forces—generated directly by the melting current—in axial and radial planes, and circumferential fluid motion

excited by an externally applied alternating magnetic field. Although a complete description of this complex physical phenomenon requires three-dimensional (3D) numerical simulations, 3D models often suffer from high computational costs and low numerical efficiency. To address this, the present study adopts a two-dimensional axisymmetric swirl model as an ideal alternative. This approach maintains computational efficiency while accurately capturing the influence of circumferential flow components on transport processes. Furthermore, by leveraging the axisymmetric nature of titanium alloy VAR ingots, the computational domain can be simplified to a semi-cross-sectional form, further significantly improving computational efficiency.

Based on this framework, the present study systematically investigates the influence of externally applied alternating magnetic fields—including magnetic field intensity and frequency—on macrosegregation behavior during the VAR process of titanium alloy ingots, using a two-dimensional axisymmetric swirl model. The computational domain for the VAR process is illustrated in Figure 1b. The ingot has a diameter of 720 mm and a final solidification height of 2.9 m. The melting current and melt rate are applied as time-dependent functions, as shown in Figure 2a. To accurately simulate the progressive solidification of the VAR ingot, a dynamic mesh technique with an element size of 10 mm was employed. The initial configuration consists of a 10 mm high liquid pool with uniformly distributed temperature and solute fields. The ingot grows along the positive x-axis.

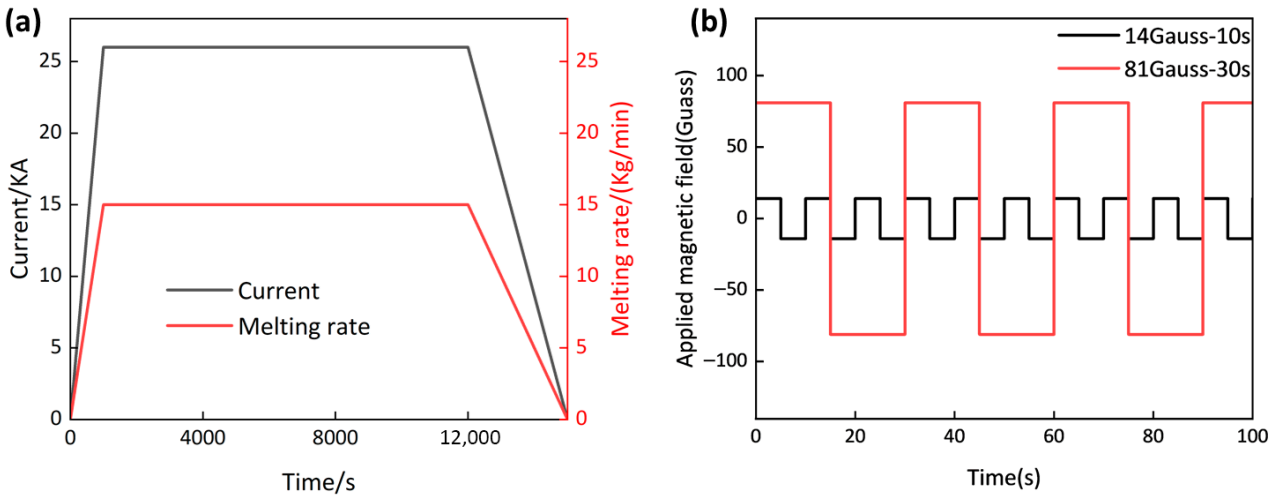


Figure 2. (**a**) Melting current and melt rate, both treated as functions of time; (**b**) two distinct patterns of applied magnetic field strength and frequency.

In this study, volume changes due to solidification shrinkage were neglected. However, the gap effect formed between the ingot and the crucible as a result of thermal contraction was taken into account. The gap begins to form when the local temperature falls below the liquidus temperature (T_L). Heat transfer between the ingot and the external copper mold is governed by thermal radiation, with the specific values calculated using Equation (9). Prior to the formation of the gap, heat transfer occurs primarily through conduction. In this study, the thermal conductivity during this stage is assumed to be constant at 800 W/m^{2}K, as illustrated in Figure 1b.

$$\lambda = \frac{\tau\left(T_{\text{ingot}}^4 - T_{\text{wall}}^4\right)}{\left(\frac{1}{\varepsilon_1} + \frac{1}{\varepsilon_2} - 1\right)\left(T_{\text{ingot}} - T_{\text{wall}}\right)} \tag{9}$$

where τ is the Stefan–Boltzmann constant with a value of 5.67×10^{-8} W·m^{-2}·K^{-4}; ε_1 and ε_2 are the thermal emissivities of the ingot surface and the inner wall of the crucible, taken

as 0.4 and 0.6, respectively. T_{ingot} and T_{wall} represent the temperature of the outer surface of the ingot and the temperature of the water-cooled mold, respectively.

The bottom of the ingot is in direct contact with the crucible wall, where a constant heat transfer coefficient of 500 W/m^{2}K is applied, as shown at the bottom boundary in Figure 1b. A combined boundary condition including both heat flux density and current density is applied on the top surface of the ingot, with the expression given as follows. The detailed derivation can be found in studies [38–41].

$$T = T_{liq} + \Delta T = T_{liq} + 400e^{-12\frac{D_{ingot}}{I_{arc}}} \tag{10}$$

$$j(r) = \frac{K_A \cdot I_{arc}}{\pi R_{arc}^2} \cdot exp(-\frac{K_B \cdot r^2}{R_{arc}^2}) \tag{11}$$

where D_{ingot} is the diameter of the ingot; I_{arc} is the melting current; R_{arc} is the electrode radius; K_A and K_B are the Gaussian distribution constants respectively.

2.3. Material Settings

The Ti-Al binary alloy was employed in this study, with relevant material parameters [43–48] summarized in Table 1. In practice, the externally applied alternating magnetic field varies not only in strength but also in periodicity. Figure 2b illustrates two distinct patterns of applied magnetic field strength and frequency variations. As indicated by the red curve, the magnetic field strength oscillates between −81 G and +81 G over a 15-s interval, completing a full reversal cycle every 30 s. This periodic variation in magnetic flux density effectively enhances fluid flow within the molten pool, thereby improving compositional homogeneity of the ingot.

Table 1. Physical parameters in this study, Adapted from Refs. [43–48].

Parameters (Symbols)	Unit	Values
Melting temperature of Ti, T_m	K	1940
Initial concentration of Al, c_0	Mol%	0.11
Density, ρ	kg/m^3	4200
Liquid slope for Al m	K/(at.%)	−416.0
Partition coefficient of Al	-	1.13
Diffusivity in Liquid, D_L	m^2/s	1.0×10^{-9}
Latent heat of fusion, L	J/kg	3.5×10^5
Solutal expansion coefficient, β	(wt%)$^{-1}$	0.4
Heat capacity, c_p	J/(kg·K)	1150
Thermal conductivity, k	W/(m·K)	30.5
Thermal expansion coefficient, β_T	K^{-1}	6.7×10^{-5}
Viscosity of liquid, ν	kg/(m·s)	0.0032
Electric conductivity, σ	S/m	1.5×10^6
Magnetic permeability, μ_0	H/m	1.26×10^{-6}

3. Results and Discussion

In this section, the reliability of the numerical model is first validated by comparing the simulated physical field distributions with literature data and matching the simulated molten pool profiles against experimental measurements. Subsequently, systematic investigations are conducted to elucidate the influence of the strength and frequency of the externally applied alternating magnetic field on ingot macrosegregation, with corresponding mechanistic interpretations provided for the observed patterns.

3.1. Model Validation

Figure 3 presents the temperature distribution, molten pool profile, and electromagnetic fields under steady-state solidification conditions at t = 10,000 s. The highest temperature is localized at the ingot top (Figure 3a), coinciding with the droplet impingement zone where significant latent heat is released. The temperature then decreases monotonically downward. Solidification initiates and proceeds as the temperature falls below the liquidus and solidus temperatures, respectively, with the fully solidified region shown in blue in Figure 3b. The molten pool exhibits a characteristic deep V-shaped profile (Figure 3b), which aligns with prior observations [10,21].

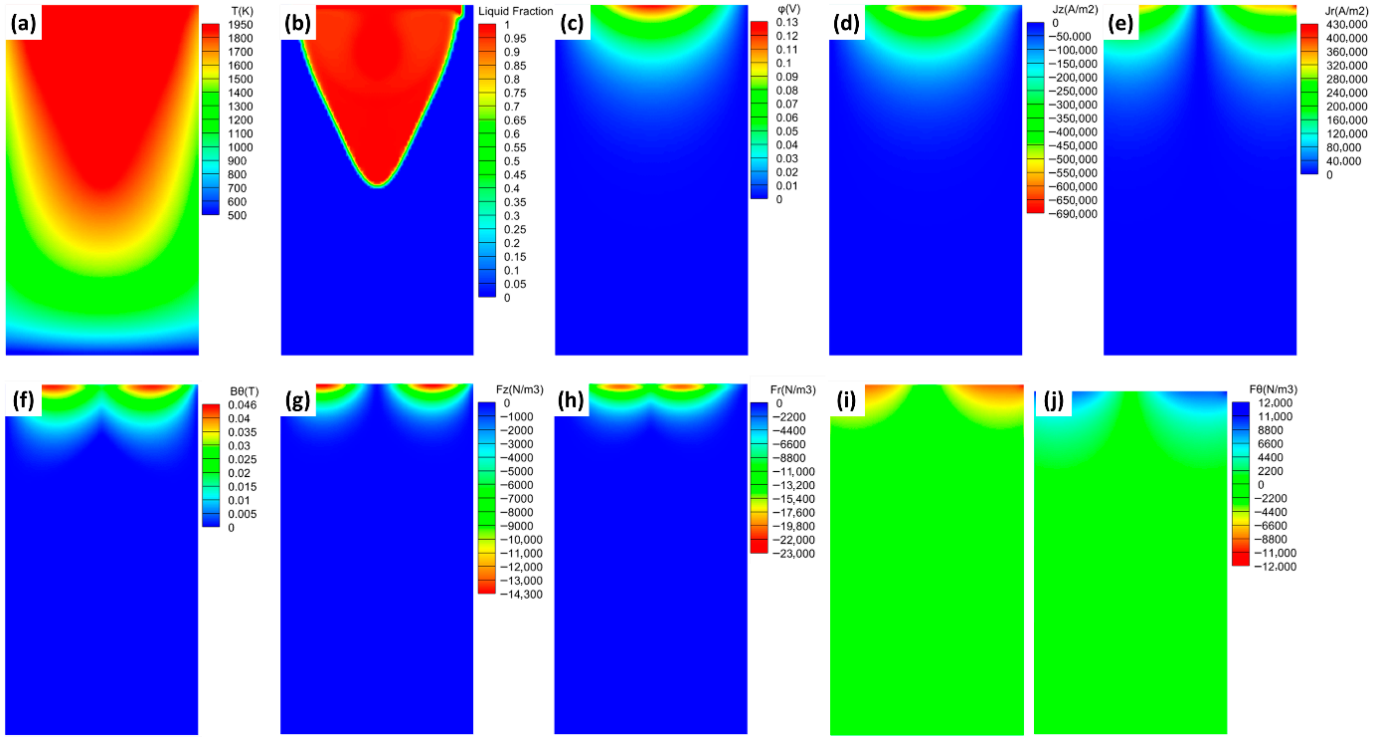


Figure 3. Simulation results of field distributions at quasi-steady state (remelting t = 10,000 s). (**a**) Temperature field. (**b**) Molten pool profile. (**c**) Electric potential field. (**d**) Axial and (**e**) radial components of the current density. (**f**) Circumferential component of the magnetic field. (**g**) Axial and (**h**) radial components of the Lorentz force. (**i**,**j**) Circumferential component of the Lorentz force at remelting times of 9800 s and 10,000 s, respectively.

The distributions of electric potential, current density, magnetic field, and Lorentz force (Figure 3c–j) agree well with previous studies [23,26]. Notably, the stirring magnetic field alternates polarity periodically (Figure 3i,j), resulting in a corresponding reversal of the Lorentz force. This alternation accurately captures the actual physical process. The overall consistency between our simulated multi-physics fields and established literature data provides preliminary validation for the model's reliability.

Figure 4a shows the pool morphology and macrostructure observed along the longitudinal section in the diameter direction of a 720 mm ingot, and the melting parameters of this ingot are shown in Figure 2b. It is worth noting that the macrostructure of the ingot was revealed by etching with hydrofluoric acid. The pool profile was determined based on the transition in the growth direction of the columnar grains, yielding a measured pool depth of 1.35 mm. To further validate the simulation, the predicted pool profile is compared against the experimental measurements in Figure 4b. The simulated profile (red curve) shows good agreement with the experimental data (black curve) in both depth and shape, confirming the reliability of the model. A slight discrepancy is observed on the right side

of the profile, likely due to the inherent asymmetry of the actual molten pool, which is not explicitly captured in the current axisymmetric model.

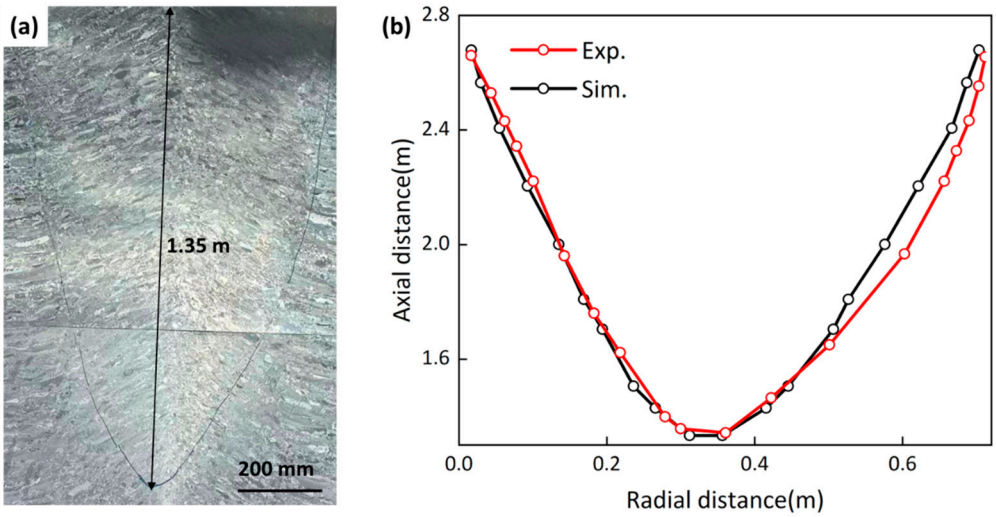


Figure 4. (**a**) Experimentally observed pool profile of a 720 mm diameter Ti-6Al alloy ingot. The melting parameters used are shown in Figure 2b. (**b**) Comparison between the simulated pool morphology, obtained using the same melting parameters as the experiment, and the experimental result.

3.2. Dependence of Macrosegregation on Alternating Magnetic Field Strength

Figure 5 clearly illustrates the influence of varying stirring magnetic field intensity on Al distribution in titanium alloy ingots. With a partition coefficient greater than unity, Al content remains relatively lower in the liquid melt during VAR according to solidification theory. This results in higher Al concentration at the initially solidified ingot bottom and lower concentration at the finally solidified top, as well as elevated levels at the early-solidified periphery and reduced levels in the late-solidified central region. These theoretical predictions show complete agreement with our simulation results. Furthermore, with increasing magnetic field strength, the positive segregation of Al at the ingot bottom and periphery progressively decreases. Simultaneously, the negative segregation in the central region exhibits a non-monotonic trend—initially intensifying before subsequently weakening with stronger magnetic fields.

Although full compositional mapping provides comprehensive homogeneity assessment, complete cross-sectional analysis of industrial-scale ingots is both economically prohibitive and inherently destructive. To maintain product yield and cost-effectiveness, the top-to-bottom concentration difference is widely used as a practical homogeneity indicator, defined as the composition at the ingot bottom minus that at the ingot top. In this paper, the top-to-bottom concentration difference is calculated as the average composition at the 10 mm position minus the average composition at the 2900 mm position. Accordingly, Table 2 summarizes the aluminum concentration ranges under different stirring magnetic field frequencies. The results clearly demonstrate that the longitudinal concentration range first increases and then decreases with increasing magnetic field strength.

Table 2. Longitudinal aluminum concentratio difference in the ingot at various magnetic field strengths.

Applied Magnetic Field	Longitudinal Aluminum Concentration Difference in the Ingot (ppm)
13Gauss-15s	3466
81Gauss-15s	3732
260Gauss-15s	3253

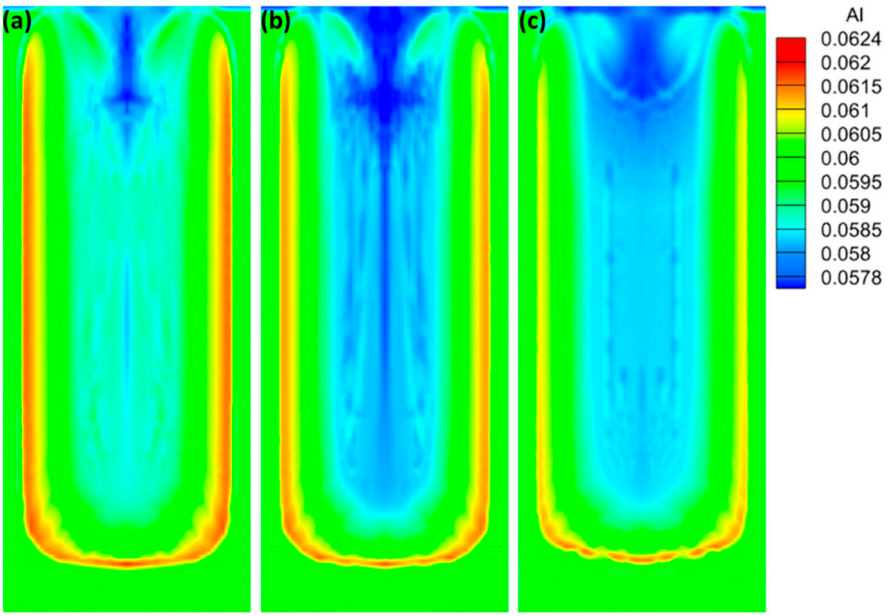


Figure 5. Aluminum distribution in the ingot (initial concentration: 6 wt.%) under an applied magnetic field with a period of 15 s at various magnetic field strengths: (**a**) 13 Gauss, (**b**) 81 Gauss, (**c**) 260 Gauss.

To elucidate the underlying mechanism governing aluminum distribution under varying stirring intensities, Figure 6 presents the molten pool flow patterns. The flow is predominantly driven by the current-induced magnetic field, exhibiting clockwise circulation on the ingot's left side and counterclockwise circulation on the right, as shown by the solid red streamlines in Figure 6. Additional weak recirculation driven by combined thermal and solutal buoyancy is observed near the pool bottom, indicated by the dashed loops at the ingot top. Notably, the applied alternating axial magnetic field generates circumferential Lorentz forces, resulting in oscillatory azimuthal flow as depicted in Figure 7. This circumferential motion induces secondary shallow recirculation in the axial-radial plane near the pool surface, clearly visible in the magnified view on the right side of Figure 6c.

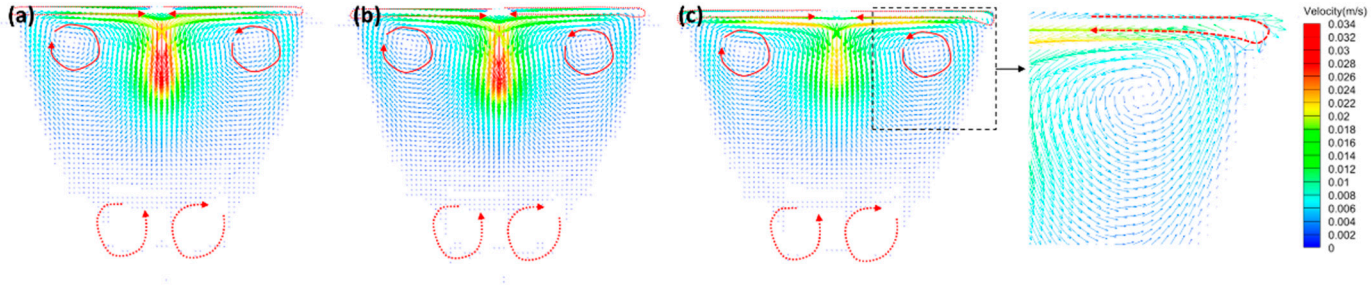


Figure 6. Fluid field distribution with a period of 15 s at various magnetic field strengths: (**a**) 13 Gauss, (**b**) 81 Gauss, (**c**) 260 Gauss.

Under weak stirring conditions (Figure 6a), the surface recirculation remains insufficient to significantly alter bulk transport. In purely diffusive regimes, a thick boundary layer enriched in depleted aluminum forms ahead of the mushy zone. The mild surface recirculation slightly agitates this boundary layer, reducing its thickness and promoting more uniform solute dispersion into the bulk liquid—achieving local homogenization. With moderate magnetic field intensification (Figure 6b), strengthened surface recirculation evolves into concentrated, penetrating vortex structures. These enhanced flows intrude into the mushy zone, eroding aluminum-depleted liquid from the solidification front. The transported solute-lean fluid is redistributed to other pool regions while being replaced by

incoming depleted liquid, significantly disturbing interfacial stability and leading to severe macroscopic segregation.

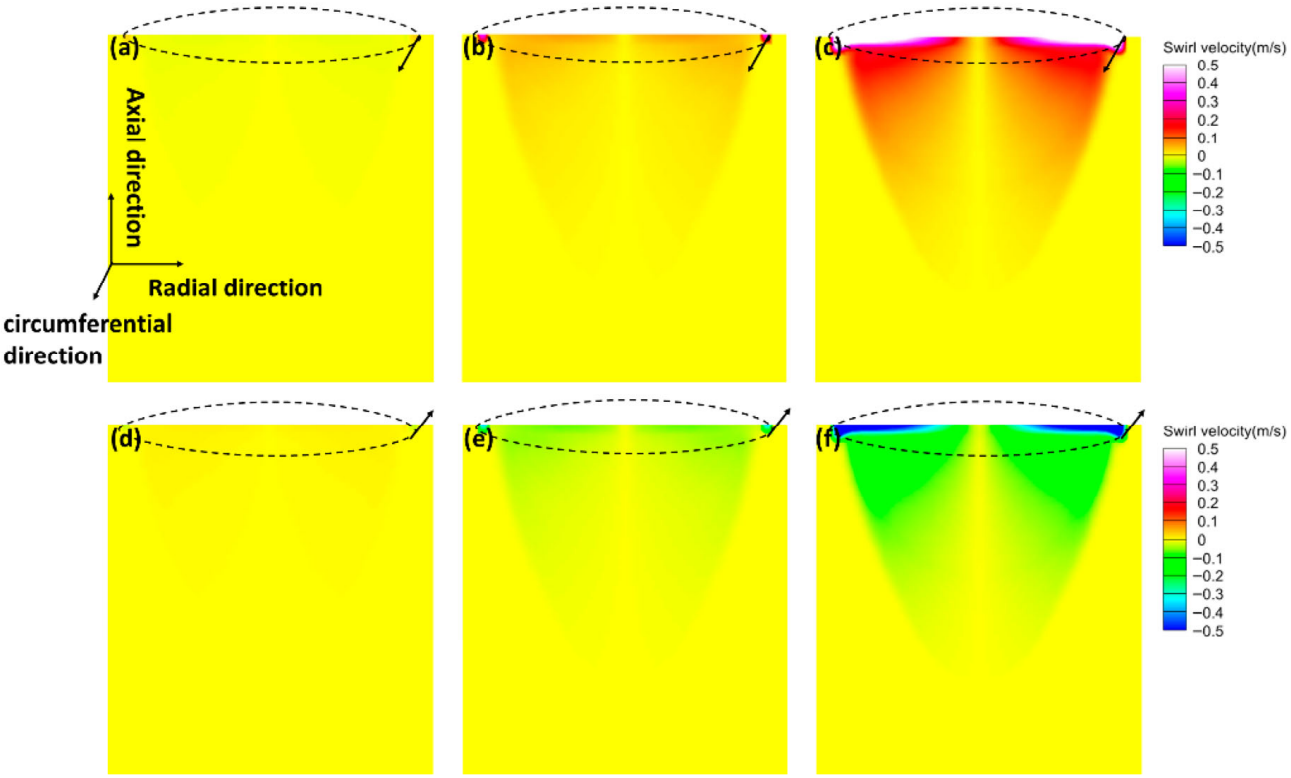


Figure 7. Circumferential flow patterns in the molten pool under an applied alternating magnetic field with a period of 15 s at various magnetic field strengths and different times: (**a**,**d**) 13 G at 10,000 s and 10,015 s, respectively; (**b**,**e**) 81 G at 10,000 s and 10,015 s, respectively; (**c**,**f**) 260 G at 10,000 s and 10,015 s, respectively.

At further increased field strengths, the surface recirculation reaches higher velocities with substantially greater kinetic energy, transitioning into fully developed turbulence. The intense turbulent mixing acts as an efficient blender, thoroughly dispersing localized solute-enriched or depleted regions formed under moderate stirring conditions. This achieves uniform solute distribution throughout the molten pool, thereby mitigating both positive peripheral segregation and negative central segregation. This optimization mechanism significantly improves ingot homogeneity and overall quality, demonstrating broad applicability for premium materials including titanium alloys and superalloys in VAR process optimization.

3.3. Dependence of Macrosegregation on Alternating Magnetic Field Frequency

Figure 8 illustrates the influence of varying frequencies of the applied stirring magnetic field on the distribution of Al element in titanium alloy ingots, while Table 3 provides a quantitative summary of the corresponding longitudinal concentration ranges. From Figure 8, it can be known that with increasing stirring frequency, the negative segregation of Al in the central region exhibits a non-monotonic trend—initially intensifying and subsequently diminishing. Specifically, at lower stirring frequencies, pronounced negative segregation is observed in the central zone; however, as the frequency increases, this segregation tendency gradually attenuates. Concurrently, the positive segregation at the ingot periphery first decreases and then increases with rising frequency. At lower frequencies, significant positive segregation is evident along the edges, which becomes less pronounced with increasing frequency, only to intensify again beyond a certain threshold.

These transitional behaviors are clearly illustrated within the black-bordered regions at the bottom of Figure 8.

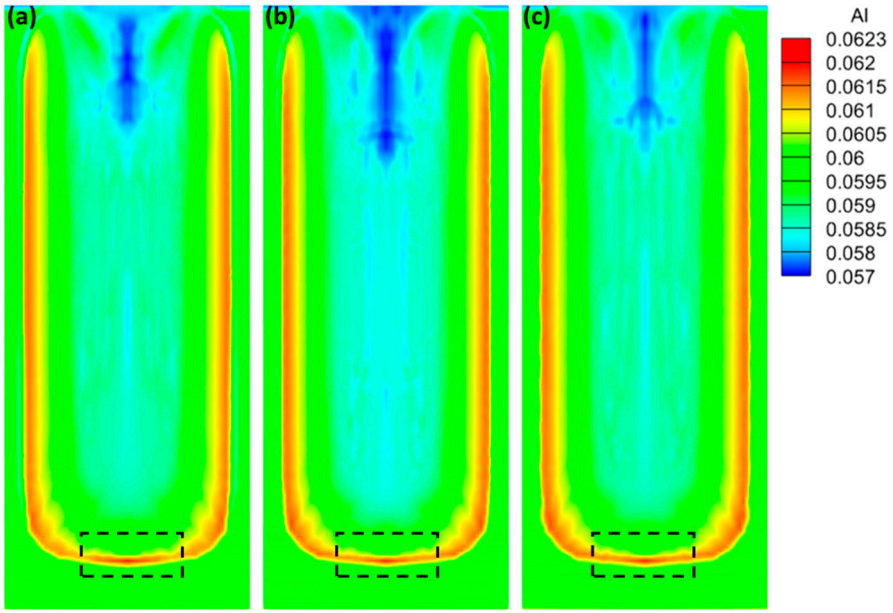


Figure 8. Al distribution in the ingot (initial concentration: 6 wt.%) under an applied magnetic field of 20 Gauss at various frequencies: (**a**) 10 s, (**b**) 60 s, (**c**) 160 s.

Table 3. Longitudinal aluminum concentration difference in the ingot at various frequencies.

Applied Magnetic Field	Longitudinal Aluminum Concentration Difference in the Ingot (ppm)
20Gauss-10s	3677
20Gauss-60s	3917
20Gauss-160s	3868

From Table 3, it is evident that the longitudinal concentration range exhibits a non-monotonic trend, initially increasing and subsequently decreasing with increasing stirring frequency. These findings underscore the significant role of the stirring magnetic field frequency in governing the distribution of Al in titanium alloy ingots. A strategic adjustment of the stirring frequency can effectively modulate Al segregation, thereby providing a viable approach to optimizing ingot homogeneity and enhancing resultant mechanical properties.

In the absence of an applied stirring magnetic field, no surface recirculation forms in the ingot pool, resulting in the mushy zone and diffusion boundary layer profiles illustrated in Figure 9a (note: only the right half of the ingot is shown). As depicted in Figure 9b, under a 20 G stirring field with a short period (10 s), the induced surface recirculation effectively thins the boundary layer—as highlighted in the blue-dashed region—thereby promoting more uniform dispersion of aluminum solute into the bulk melt.

With increasing stirring period, prolonged unidirectional recirculation gradually penetrates the mushy zone, as shown in Figure 9c, eroding the aluminum-depleted liquid from the solidification front. This solute-lean liquid is subsequently transported to other regions of the pool via circulating flow. Such interaction disturbs the stability of the solidification front and leads to deterioration of ingot homogeneity.

As the stirring period increases, sustained unidirectional recirculation gradually penetrates the mushy zone, as shown in Figure 9c, generating strong shear forces across the entire solidification front. This leads to a significant and uniform reduction in the thickness

of the diffusion boundary layer. A thinner boundary layer enhances the mass transfer coefficient, enabling efficient solute exchange between the growing solid and the bulk melt. Consequently, any localized aluminum-rich or aluminum-lean regions formed during the intermediate stages are rapidly dispersed and homogenized by the intense flow, achieving a uniform solute concentration throughout the molten pool.

When the stirring period is further extended to a sufficiently long duration (Figure 9d), sustained surface recirculation directly interacts with the mushy zone, functioning as a highly efficient mixer. This stirring mechanism thoroughly disperses and homogenizes localized aluminum-rich or aluminum-lean regions formed under intermediate periods, achieving uniform solute concentration throughout the molten pool. As a result, macrosegregation in the final ingot is significantly reduced.

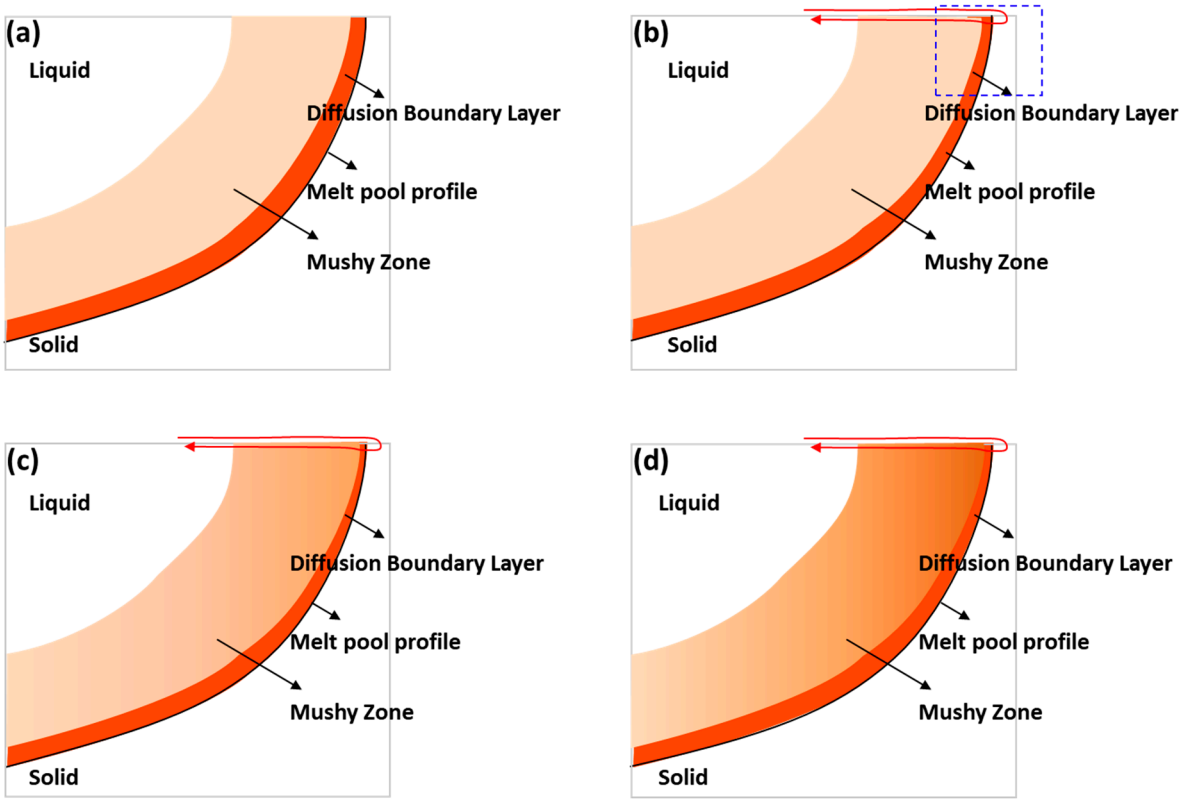


Figure 9. Schematic illustration of the diffusion boundary layer and mushy zone under varying stirring periods: (**a**) Without applied magnetic field; (**b**) With 20 G stirring field at 10 s period; (**c**) With 20 G stirring field at 60 s period; (**d**) With 20 G stirring field at 160 s period.

This study demonstrates that both the intensity and period of the stirring magnetic field considerably influence solute distribution homogeneity. Through rational adjustment of these parameters, flow patterns within the pool can be effectively controlled, thereby optimizing the compositional uniformity of the ingot.

4. Conclusions

This study develops a validated multi-physics model coupling electromagnetic, flow, temperature, and solute fields to analyze how alternating magnetic fields affect macrosegregation in titanium alloy VAR ingots. Key findings reveal that both magnetic field intensity and period significantly influence segregation through flow-induced mechanisms.

Results demonstrate optimal ranges for both intensity and period. For a Ti-6Al ingot with a diameter of 720 mm, increasing the magnetic field strength from 13 G to 81 G initially reduces homogeneity, while a further increase to 260 G improves it. To minimize

the top-to-bottom concentration difference, the optimal magnetic field strength range is determined to be either below 13 G or around 260 G, depending on the period. Regarding the magnetic field period, under a fixed intensity of 20 G, a short period of 10 s results in poor ingot homogeneity, a medium period of 60 s further deteriorates homogeneity, whereas a long period of 160 s improves it.

The core mechanism involves magnetic-field-induced recirculation near the pool surface. Weak recirculation thins diffusion boundary layers, enhancing homogeneity. Moderate recirculation disturbs solidification front stability, increasing segregation. Strong recirculation creates complete mixing, achieving uniform solute distribution. Similarly, short periods maintain thin boundary layers via frequent flow reversal, while medium periods cause interfacial instability through sustained unidirectional flow. Sufficiently long periods enable complete homogenization through prolonged mixing.

These findings provide theoretical guidance for optimizing electromagnetic stirring parameters to enhance compositional uniformity in titanium alloy ingots.

Author Contributions: Conceptualization, M.J., Y.W., L.H. and X.L.; Methodology, M.J. and Y.W.; Software, M.J.; Validation, M.J., Q.W., J.F., Z.L. and X.L.; Formal analysis, M.J. and J.F.; Investigation, M.J. and T.H.; Resources, M.J., T.H. and X.L.; Data curation, M.J., Q.W., J.S. and K.W.; Writing—original draft, M.J.; Writing—review & editing, M.J.; Visualization, M.J. and Z.L.; Supervision, M.J., J.S., L.H., K.W. and X.L.; Project administration, M.J. All authors have read and agreed to the published version of the manuscript.

Funding: This research received no external funding.

Data Availability Statement: The original contributions presented in this study are included in the article. Further inquiries can be directed to the corresponding author.

Acknowledgments: This work acknowledges the computational time and facilities provided by the Xi'an Supercomputing Center and High Performance Computing Center in China.

Conflicts of Interest: Authors Meirong Jiang, Yulun Wu, Qing Wang, Jie Fu, Jinjin Shang, Tao He, Longchao Huang and Kaixuan Wang were employed by the Western Superconducting Technologies Co., Ltd. The remaining authors declare that the research was conducted in the absence of any commercial or financial relationships that could be construed as a potential conflict of interest.

References

1. Wu, Z.Y.; Liu, Y.J.; Wu, X.; Liu, X.C.; Wang, J.C.; Wang, Q. Fatigue performance of beta titanium alloy topological porous structures fabricated by laser powder bed fusion. *J. Mater. Res. Technol.* **2024**, *29*, 4772–4780. [CrossRef]
2. Veiga, C.; Davim, J.P.; Loureiro, A.J.R. Properties and applications of titanium alloys: A brief review. *Rev. Adv. Mater. Sci.* **2012**, *32*, 14–34.
3. Bache, M. Titanium alloys: Processing and properties. *Metals* **2021**, *11*, 1426. [CrossRef]
4. Finlay, W.L.; Snyder, J.A. Effects of three interstitial solutes (nitrogen, oxygen, and carbon) on the mechanical properties of high-purity, alpha titanium. *JOM* **1950**, *188*, 277–286. [CrossRef]
5. Yankov, E.; Nikolova, M.P.; Dechev, D.; Ivanov, N.; Hikov, T.; Valkov, S.; Dimitrova, V.; Yordanov, M.; Petrov, P. Changes in the Mechanical Properties of Ti Samples with TiN and TiN/TiO_2 coatings deposited by different PVD methods. *IOP Conf. Ser. Mater. Sci. Eng.* **2018**, *416*, 012062. [CrossRef]
6. Zhang, Z.; Zhang, Y.; Zhang, Z.; He, G. Effect of brittle TiN coating on fatigue performance of TC11 titanium alloy under rotating bending and tension-tension. *J. Alloys Compd.* **2023**, *968*, 172163. [CrossRef]
7. Huang, X.; Du, K.; Zhu, Y.; Xu, H.; Liu, Z.; Wang, F.; Li, B.; Geng, Y. Study on solidification and macrosegregation of aluminium and titanium in the electroslag remelted ingots of K500 alloy. *J. Mater. Res. Technol.* **2025**, *39*, 5027–5036. [CrossRef]
8. Campbell, J. A future for vacuum arc remelting and electroslag remelting—A critical perspective. *Metals* **2023**, *13*, 1634. [CrossRef]
9. Karimi-Sibaki, E.; Peyha, M.; Vakhrushev, A.; Wu, M.; Ludwig, A.; Bohacek, J.; Preiss, B.; Kharicha, A. Experimental and numerical investigations of arc plasma expansion in an industrial vacuum arc remelting (VAR) process. *Sci. Rep.* **2022**, *12*, 20405. [CrossRef]
10. Karimi-Sibaki, E.; Kharicha, A.; Wu, M.; Ludwig, A.; Bohacek, J. A parametric study of the vacuum arc remelting (VAR) process: Effects of arc radius, side-arcing, and gas cooling. *Metall. Mater. Trans. B* **2020**, *51*, 222–235. [CrossRef]

11. Yun, P.F.; Cao, J.H.; Shi, Y.H.; Liu, H.; Wu, Y.K.; Jiang, F. Macrosegregation in vacuum arc remelted Ti-4.7Al-3V-2Mo-1.85Fe alloy: Industrial-scale ingot and numerical simulation. *J. Mater. Eng. Perform.* **2025**, *34*, 20598–20613. [CrossRef]
12. Guan, J.; Miao, Y.; Chen, Z.; Liu, D.-R.; Cao, Y.; Li, D. Modeling of macrosegregation formation and the effect of enhanced cooling during vacuum arc remelting solidification of NbTi alloy ingot. *Metall. Mater. Trans. B* **2022**, *53*, 4048–4062. [CrossRef]
13. Dobatkin, V.I.; Anoshkin, N.F. Comparison of macrosegregation in titanium and aluminium alloy ingots. *Mat. Sci. Eng. A* **1999**, *263*, 224–229. [CrossRef]
14. Yin, X.; Liu, J.; Wang, Q.; Li, W.; Deng, H.; Wang, Z.; Luo, H.; Li, W. Quantitative characterization of beta fleck segregation in a Ti–17 alloy ingot produced by vacuum arc remelting without electromagnetic stirring. *Met. Mater. Int.* **2024**, *31*, 2123–2135. [CrossRef]
15. Mitchell, A.; Kawakami, A.; Cockcroft, S.L. Segregation in titanium alloy ingots. *High. Temp. Mater. Process.* **2007**, *26*, 59–78. [CrossRef]
16. Davidson, P.A.; He, X.; Lowe, A.J. Flow transitions in vacuum arc remelting. *Mater. Sci. Technol.* **2000**, *16*, 699–711. [CrossRef]
17. Xu, C.; Zhang, H.; Gomes-Rodrigues, C.; Kharicha, A.; Wu, M. Importance of buoyancy flow in the macrosegregation formation during solidification of VAR process. *IOP Conf. Ser. Mater. Sci. Eng.* **2025**, *1335*, 012021. [CrossRef]
18. Zagrebelnyy, D.; Krane, M.J.M. Segregation development in multiple melt vacuum arc remelting. *Metall. Mater. Trans. B* **2009**, *40*, 281–288. [CrossRef]
19. Davidson, P.A.; Kinnear, D.; Lingwood, R.J.; Short, D.J.; He, X. The role of Ekman pumping and the dominance of swirl in confined flows driven by Lorentz forces. *Eur. J. Mech. B Fluids* **1999**, *18*, 693–711. [CrossRef]
20. Chapelle, P.; Jardy, A.; Bellot, J.P.; Minvielle, M. Effect of electromagnetic stirring on melt pool free surface dynamics during vacuum arc remelting. *J. Mater. Sci.* **2008**, *43*, 5734–5746. [CrossRef]
21. Xiong, Y.; Liu, Z.; Wang, F.; Zhao, Z.; Tan, H.; Baleta, J.; Li, B. Effect of magnetic field on molten pool behavior in vacuum arc remelting process of large-sized titanium alloy ingot. *J. Iron Steel Res. Int.* **2025**, *32*, 2771–2783. [CrossRef]
22. Li, D.; Sun, D.; Li, J.; Chen, S. Lattice Boltzmann-large eddy simulation modeling of heat transfer and solute segregation during vacuum arc remelting under an external magnetic field. *Int. Commun. Heat Mass Transf.* **2025**, *169*, 109849. [CrossRef]
23. Li, J.; Li, P.; Guo, J.; Xu, C.; Wang, J.; Huang, L.; Fan, K. Multiscale simulation of the effect of axial magnetic field on macrosegregation and solidification structure during vacuum arc remelting of TC17. In Proceedings of the 75th World Foundry Congress, Deyang, China, 25–30 October 2024; pp. 281–282.
24. Karimi-Sibaki, E.; Vakhrushev, A.; Wu, M.; Bohacek, J.; Kharicha, A. A numerical study on effects of current density distribution, turbulence, and magnetohydrodynamics (MHD) on electrolytic gas flow with application to alkaline water electrolysis (AWE). *Chem. Eng. Res. Des.* **2024**, *208*, 731–739. [CrossRef]
25. Karimi-Sibaki, E.; Kharicha, A.; Abdi, M.; Vakhrushev, A.; Wu, M.; Ludwig, A.; Bohacek, J. A numerical study on the influence of an axial magnetic field (AMF) on vacuum arc remelting (VAR) process. *Metall. Mater. Trans. B* **2021**, *52*, 3354–3362. [CrossRef]
26. Xu, C.; Guo, J.; Wang, J.; Li, J.; Huang, L.; Fan, K.; Zhang, H.; Wu, M. Numerical investigation of axial magnetic field effects on melt flow and macrosegregation in TC17 alloy vacuum arc remelting. In *Proceedings of the 8th International Conference on Solidification and Gravity 2024*; Roósz, A., Veres, Z., Eds.; BP International: West Bengal, India, 2024; pp. 41–53. [CrossRef]
27. Han, J.; Ren, N.; Zhou, Y.; Zhang, R.; Li, J.; Huang, X.; Li, J. Melt convection and macrosegregation in the vacuum arc remelted Ti_2AlNb ingot: Numerical methods and experimental verification. *J. Mater. Proc. Technol.* **2022**, *308*, 117729. [CrossRef]
28. Guan, J.; Liu, D.-R.; Cao, Y.; Liu, H.; Fu, P.; Liu, H.; Sun, C.; Miao, Y.; Li, D. Macro and micro segregations and prediction of carbide equivalent size in vacuum arc remelting of m50 steel via simulations and experiments. *Metall. Mater. Trans. A* **2024**, *55*, 1081–1097. [CrossRef]
29. Sun, Z.; Xia, Z.; Zhang, M.; Guo, Y.; Ma, C.; Deng, G.; Zheng, T.; Shen, Z.; Ding, B.; Li, Q.; et al. The effect of alternative magnetic field on solidification structure improvement and primary carbide refinement in M50 ingots produced by vacuum arc remelting. *J. Mater. Res. Technol.* **2024**, *30*, 5219–5231. [CrossRef]
30. Mramor, K.; Quatravaux, T.; Combeau, H.; Jardy, A.; Založnik, M.; Crassous, I.; Gaillac, A. On the prediction of macrosegregation in vacuum arc remelted ingots. *Metall. Mater. Trans. B* **2022**, *53*, 2953–2971. [CrossRef]
31. Li, M.; Jia, L.; Miao, Q.; Liu, W.; Zhao, P.; Yang, S. Numerical simulation of arc stabilizing cycle in vacuum arc remelting of titanium alloy. *Phys. Scr.* **2024**. [CrossRef]
32. Pericleous, K.; Djambazov, G.; Ward, M.; Yuan, L.; Lee, P.D. A multiscale 3D model of the vacuum arc remelting process. *Metall. Mater. Trans. A* **2013**, *44*, 5365–5376. [CrossRef]
33. Woodside, C.R.; King, P.E.; Nordlund, C. Arc distribution during the vacuum arc remelting of Ti-6Al-4V. *Metall. Mater. Trans. B* **2013**, *44*, 154–165. [CrossRef]
34. Yuan, L.; Djambazov, G.; Lee, P.D.; Pericleous, K. Multiscale modeling of the vacuum arc remelting process for the prediction on microstructure formation. *Int. J. Mod. Phys. B* **2009**, *23*, 1584–1590. [CrossRef]
35. Xiong, Y.; Liu, Z.; Zhao, Z.; Li, B. Numerical investigation on the evolution behavior of solidification structure in titanium alloy during vacuum arc remelting process. *Metall. Mater. Trans. B* **2024**, *55*, 4182–4199. [CrossRef]

36. Yang, S.; Tian, Q.; Yu, P.; Yang, S.; Liu, W.; Li, J. Numerical simulation and experimental study of vacuum arc remelting (VAR) process for large-size GH4742 superalloy. *J. Mater. Res. Technol.* **2023**, *24*, 2828–2838. [CrossRef]
37. Yang, Z.; Zhao, X.; Kou, H.; Li, J.; Hu, R.; Zhou, L. Numerical simulation of temperature distribution and heat transfer during solidification of titanium alloy ingots in vacuum arc remelting process. *Trans. Nonferrous Met. Soc. China* **2010**, *20*, 1957–1962. [CrossRef]
38. Bennon, W.D.; Incropera, F.P. A continuum model for momentum, heat and species transport in binary solid-liquid phase change systems—I. Model formulation. *Int. J. Heat Mass Transf.* **1987**, *30*, 2161–2170. [CrossRef]
39. Bennon, W.D.; Incropera, F.P. A continuum model for momentum, heat and species transport in binary solid-liquid phase change systems—II. Application to solidification in a rectangular cavity. *Int. J. Heat Mass Transf.* **1987**, *30*, 2171–2187. [CrossRef]
40. Bellet, M.; Combeau, H.; Fautrelle, Y.; Gobin, D.; Rady, M.; Arquis, E.; Budenkova, O.; Dussoubs, B.; Duterrail, Y.; Kumar, A.; et al. Call for contributions to a numerical benchmark problem for 2D columnar solidification of binary alloys. *Int. J. Therm. Sci.* **2009**, *48*, 2013–2016. [CrossRef]
41. Prakash, C.; Voller, V. On the numerical solution of continuum mixture model equations describing binary solid-liquid phase change. *Numer. Heat Transf. Part B Fundam.* **1989**, *15*, 171–189. [CrossRef]
42. Voller, V.R.; Prakash, C. A fixed grid numerical modelling methodology for convection-diffusion mushy region phase-change problems. *Int. J. Heat Mass Transf.* **1987**, *30*, 1709–1719. [CrossRef]
43. Zhang, F.; Chen, S.L.; Chang, Y.A.; Kattner, U.R. A thermodynamic description of the Ti-Al system. *Intermetallics* **1997**, *5*, 471–482. [CrossRef]
44. Thiyaneshwaran, N.; Selvan, C.P.; Lakshmikanthan, A.; Sivaprasad, K.; Ravisankar, B. Comparison based on specific strength and density of in-situ Ti/Al and Ti/Ni metal intermetallic laminates. *J. Mater. Res. Technol.* **2021**, *14*, 1126–1136. [CrossRef]
45. Watanabe, M.; Funada, S.; Ohtsuka, M.; Adachi, M.; Fukuyama, H. Density, normal spectral emissivity, heat capacity, and thermal conductivity of the ti6al4v melt measured by electromagnetic levitation with a static magnetic field. *Int. J. Thermophys.* **2025**, *46*, 52. [CrossRef]
46. Zhou, K.; Wang, H.P.; Wei, B. Determining thermophysical properties of undercooled liquid Ti–Al alloy by electromagnetic levitation. *Chem. Phys. Lett.* **2012**, *521*, 52–54. [CrossRef]
47. Mishin, Y.; Herzig, C. Diffusion in the Ti–Al system. *Acta Mater.* **2000**, *48*, 589–623. [CrossRef]
48. Dong, R.-E.; Assari, A.H.; Yaghoobi, S.; Mahmoodi, M.; Ghaderi, S. Effect of volume fraction of Ti on microstructure evolution and thermal properties of Al/Ti laminated composites. *Met. Mater. Int.* **2024**, *30*, 1002–1014. [CrossRef]

Disclaimer/Publisher's Note: The statements, opinions and data contained in all publications are solely those of the individual author(s) and contributor(s) and not of MDPI and/or the editor(s). MDPI and/or the editor(s) disclaim responsibility for any injury to people or property resulting from any ideas, methods, instructions or products referred to in the content.